



Magnetron-sputtered and thermal-evaporated low-loss Sb-Se phase-change films in non-volatile integrated photonics

KUNHAO LEI,^{1,5} MAOLIANG WEI,^{1,5} ZEQUAN CHEN,^{2,3,5} JIANGHONG WU,^{2,3} JIALING JIAN,^{2,3} JIA DU,⁴ JUNYING LI,^{1,6} LAN LI,^{2,3,7}  AND HONGTAO LIN¹ 

¹State Key Laboratory of Modern Optical Instrumentation, College of Information Science and Electronic Engineering, Zhejiang University, Hangzhou 310027, China

²Key Laboratory of 3D Micro/Nano Fabrication and Characterization of Zhejiang Province, School of Engineering, Westlake University, Hangzhou, Zhejiang 310024, China

³Institute of Advanced Technology, Westlake Institute for Advanced Study, Hangzhou, Zhejiang 310024, China

⁴Key Laboratory of Optical Technology and Instrument for Medicine, Ministry of Education, University of Shanghai for Science and Technology, Shanghai 200093, China

⁵These authors contributed equally to this work

⁶junyingli@zju.edu.cn

⁷lilan@westlake.edu.cn

Abstract: Chalcogenide phase change materials (PCMs), featuring a large contrast in optical properties between their non-volatile amorphous and crystalline states, have triggered a surge of interest for their applications in ultra-compact photonic integrated circuits with long-term near-zero power consumption. Over the past decade, however, PCM-integrated photonic devices and networks suffered from the huge optical loss of various commonly-used PCMs themselves. In this paper, we focused on the deposition, characterization, and monolithic integration of an emerging low-loss phase change material, Sb₂Se₃ on a silicon photonic platform. The refractive index contrast between the amorphous and crystalline phase of the evaporated Sb-Se thin film was optimized up to 0.823 while the extinction coefficient remains less than 10⁻⁵ measured by ellipsometry. When integrated on a silicon waveguide, the propagation loss introduced by the amorphous thin film is negligibly low. After crystallization, the propagation loss of a magnetron-sputtered Sb-Se patch-covered silicon waveguide is as low as 0.019 dB/μm, while its thermal-evaporated counterpart is below 0.036 dB/μm.

© 2022 Optica Publishing Group under the terms of the [Optica Open Access Publishing Agreement](#)

1. Introduction

Chalcogenide phase change materials (PCMs) are a type of materials that presents large optical contrast along with their non-volatile phase transition [1–3]. Compared with traditional thermo-optical and electro-optical switches, the energy consumption of reconfigurable photonic devices based on these PCMs occurs only during the phase switching process. On the other hand, the obvious modulation effect resulting from the large optical contrast of PCMs helps reduce the system's footprint and overall power consumption. Therefore, chalcogenide PCMs are considered to be a CMOS-compatible solution to integrated photonic circuits with compact size and non-volatile reconfigurability [4,5].

In recent years, non-volatile optical switches [6–9], integrated photonic memories [10–13], optical neural networks [14–17], and metasurfaces [18–21] based on chalcogenide-PCMs have been demonstrated. However, in these photonic devices, the widely used chalcogenide PCM Ge₂Sb₂Te₅ suffers from its high absorption loss (up to 7.6 dB/μm for the crystalline state) in

the communication band [22]. Although efforts to increase the optical bandgap and mitigate the optical absorption of chalcogenide PCMs in the near-infrared band [23] have been made by substituting Te atoms with Se atoms in $\text{Ge}_2\text{Sb}_2\text{Te}_5$, this type of chalcogenide PCMs, i.e. GeSbSeTe , still exhibits a high optical loss at 1550 nm wavelength. Recently, a new family of ultra low-loss chalcogenide PCMs including Sb_2Se_3 and Sb_2S_3 has been reported [24]. These materials exhibit an extinction coefficient κ of less than 10^{-4} at C-band and O-band in both amorphous and crystalline phases. Between these two PCMs, Sb_2Se_3 presents a lower crystallization temperature (200 °C) and a larger refractive index contrast ($\Delta n = 0.77$) at 1550 nm wavelength. Meanwhile, the propagation loss of a Sb_2Se_3 -covered SiN_x waveguide [24] is claimed to be as low as 0.07 dB/ μm when Sb_2Se_3 is in its high-loss crystalline state. These demonstrations make Sb_2Se_3 an anticipated low-loss PCM candidate for non-volatile phase-modulation in photonic circuits.

Magnetron sputtering is one of the most commonly used thin film deposition techniques to integrate Sb_2Se_3 PCM onto photonic waveguides. However, different deposition techniques often lead to differences in morphology and chemical composition of the film, which could significantly affect the structural and optical properties of PCMs. Therefore, thin-film deposition techniques matter in the performance of PCM-integrated hybrid waveguides, yet they have hardly ever been studied. In this paper, we prepared Sb-Se thin films by magnetron sputtering and thermal evaporation, respectively. The effect of the two deposition processes on thin-film chemical composition, morphology, and optical properties of the Sb-Se material system was investigated via atomic force microscope (AFM), scanning electron microscope (SEM), X-ray diffraction (XRD), X-ray photoelectron spectroscopy (XPS) and ellipsometry. Furthermore, we integrated the Sb-Se PCMs with microring resonators to characterize their modulation performance and optical loss quantitatively.

2. Fabrication

RF magnetron sputtering system (Beijing Technol Science Co. Ltd.) with a 3 in. Sb_2Se_3 target was employed to deposit phase-change thin films. Ar flow with a rate of 40 sccm entered the chamber when the base pressure reached 5.0×10^{-4} Pa. Magnetron-sputtered Sb-Se (MS-SbSe) films were sputtered with an optimized power of 50 W under a working pressure of 0.5 Pa after 15-min pre-sputtering to remove contaminants from the target surface.

Thermal-evaporated Sb-Se (TE-SbSe) thin films were evaporated from 99.999% pure Sb_2Se_3 powder (Alfa Aesar Co. Ltd.) at a base pressure of 5.0×10^{-4} Pa. The deposition rate was stabilized at 7-8 Å/s.

Sb-Se-integrated photonic devices were fabricated on 220 nm SOI wafers with a 2- μm -thick SiO_2 box layer by combining the multi-project-wafer (MPW) process with electron beam lithography (EBL) [25,26]. Firstly, the device structures were defined by deep ultra-violet (DUV) photolithography and inductive coupling plasma (ICP) etching process at the Institute of Microelectronics of the Chinese Academy of Sciences (IMECAS). Then, the phase-change layer pattern was defined by EBL, followed by the integration of 30-nm-thick Sb-Se patches onto the waveguides of microring resonators by a lift-off process.

3. Result and discussion

Figures 1(a) and (d) show the SEM images of an MS- and TE-SbSe PCM patch integrated on a single-mode silicon microring resonator, respectively. These microring resonators possess a radius of 40 μm , a width of 500 nm and an etching depth of 150 nm. The PCM patches have a width of 3 μm and a length ranging from 5 μm to 45 μm . When phase change of Sb-Se takes place, the effective index of the PCM-covered waveguide changes, leading to a shift in the microring's resonance dip.

As-deposited Sb-Se films are amorphous, and the sputtered films (see the AFM image in Fig. 1 (b)) have coarser surfaces than the TE-SbSe ones (see the Fig. 1 (e)). The crystallization of

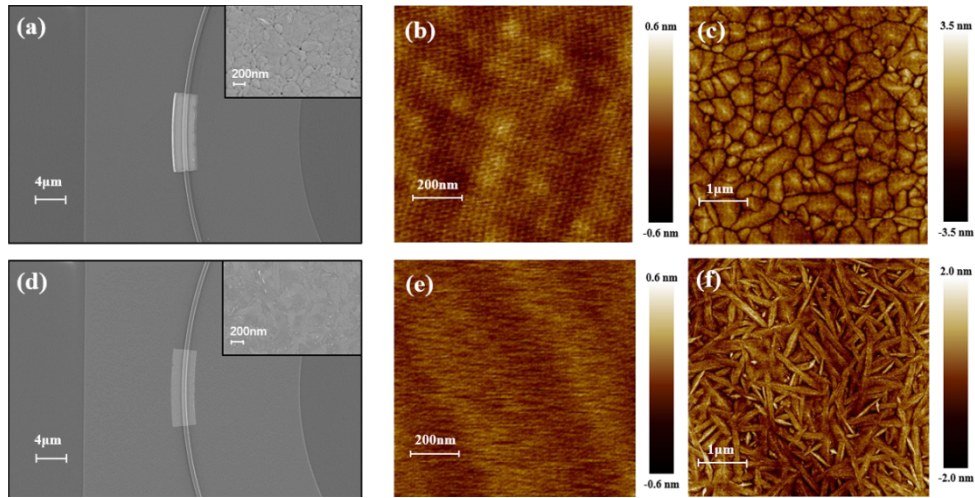


Fig. 1. SEM and AFM images of the fabricated microring waveguides and Sb-Se thin films. (a), (d) microring resonators integrated with PCM patches deposited by magnetron sputtering and thermal evaporation, respectively. (b), (e) the AFM images of the amorphous Sb-Se deposited by magnetron sputtering and thermal evaporation, respectively. (c), (f) the AFM images of the crystalline Sb-Se deposited by magnetron sputtering and thermal evaporation, respectively.

as-deposited amorphous Sb-Se films on photonic devices was achieved by thermal annealing at 200 °C in a nitrogen atmosphere for 30 min. After the annealing-induced crystallization, crystals in the TE-SbSe film tend to be disordered and nanorod-like (see Fig. 1(f)), while the crystal morphology of the MS-SbSe film is more regular and uniform (see Fig. 1(c)).

To determine the differences between Sb-Se films deposited via two different techniques, we conducted X-ray diffraction to analyze the Sb-Se thin films annealed at 200 °C, as shown in Fig. 2(a). Both MS- and TE-SbSe thin films show orthorhombic phase, corresponding to JCPDS standard card 15-0861 [27]. A weak diffraction peak at 30° in TE-SbSe thin films was speculated to be related to a very low amount of Sb phase (according to JCPDS card 26-0101) [28].

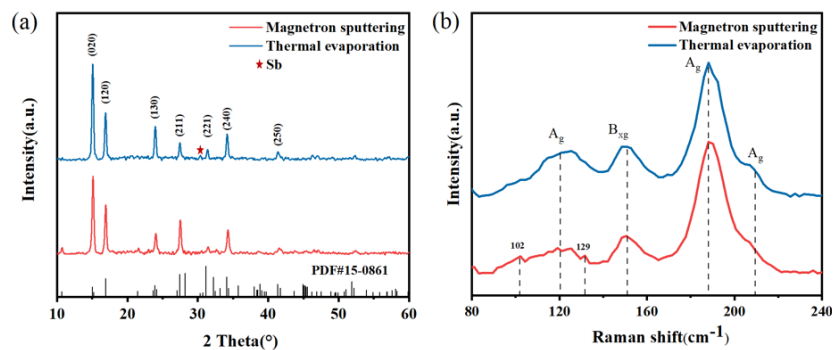


Fig. 2. (a) X-ray diffraction spectra of crystalline Sb-Se deposited by magnetron sputtering and thermal evaporation. (b) Raman spectroscopy for Sb-Se deposited by magnetron sputtering and thermal evaporation after annealing at 200 °C.

To further investigate the crystallinity and structure of the above crystallized thin films, Raman spectra were acquired using a 638 nm laser (Fig. 2(b)). The spectra of crystallized MS- and

TE-SbSe thin films both contain vibrational modes of symmetry groups A_g at 188, 210, 120 cm^{-1} , B_g at 150 cm^{-1} in Fig. 2(b) [29]. Among them, the sharpest peak at 188 cm^{-1} is pointed as the stretching mode of Sb-Se bonds, peaks at 120, and 210 cm^{-1} are associated with Se-Se bonds, and the peak at 150 cm^{-1} is related to the vibration of Sb-Sb bonds [30–32]. The spectra for the Se-rich region show additional peaks close to 102 cm^{-1} and 129 cm^{-1} for crystallized MS-SbSe thin films, which are related to weak vibration modes of the rhombohedral crystal structure of selenium [33].

XRD and Raman characterizations suggest that MS- and TE-SbSe thin films might be Se-rich and Sb-rich, respectively. To verify this hypothesis, we analyze the constituent element oxidation state of MS- and TE-SbSe thin films by X-ray photoelectron spectroscopy. It can be seen from Fig. 3 that the two processes have a similar spectrum. For MS-SbSe thin films, the main Sb 3d_{5/2} peak is at 529.3 eV, consistent with the published literature [29,34–36]. The small metal Sb peak is at 527.9 eV and the oxide peak is at 530.35 eV. The O 1s peak appears shifted at 531 eV, while the main Se 3d_{5/2} peak is at 53.7 eV. The atomic percentage of Sb 3d_{5/2} is 33.23% and Se 3d_{5/2} is 66.77%, which agrees with the result of Raman spectroscopy verifying that MS-SbSe thin films are Se-rich due to the preferential sputtering. The selenium elemental peaks appearing at 54.7 eV and 55.3 eV result from rhombohedral Se crystal in the magnetron sputtered thin films, in accordance with what showed by Raman spectroscopy. As for TE-SbSe thin films, the main Sb 3d_{5/2} peak is at 529.5 eV, while the main Se 3d_{5/2} peak is at 54.0 eV. The atomic percentage of Sb 3d_{5/2} is 50.09% and Se 3d_{5/2} is 49.91%, which is consistent with X-Ray diffraction patterns, indicating that TE-SbSe thin films are Sb-rich. This may result from the lower vapor pressure of Sb during the thermal deposition process [37,38].

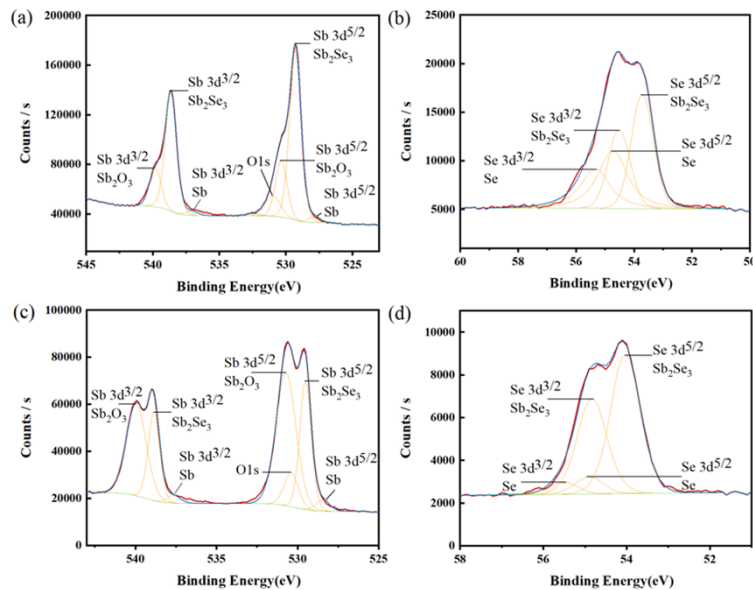


Fig. 3. X-ray photoelectron spectroscopy of (a) Sb 3d, (b) Se 3d deposited by magnetron sputtering, and (c) Sb 3d, (d) Se 3d deposited by thermal evaporation.

For PCMs in photonic devices, optical contrast between amorphous and crystalline phases is a critical characteristic. Figure 4 shows the refractive index (n) and extinction coefficient (k) of Sb-Se thin films obtained by ellipsometry. At 1550 nm wavelength, MS-SbSe thin films present a refractive index contrast of 0.575, while TE-SbSe thin films claim a record refractive index contrast of 0.823. Meanwhile, the extinction coefficient of the films deposited by both methods is

less than 10^{-5} in the communication band, suggesting that SbSe could be a high-performance phase-modulation-only non-volatile optical PCM.

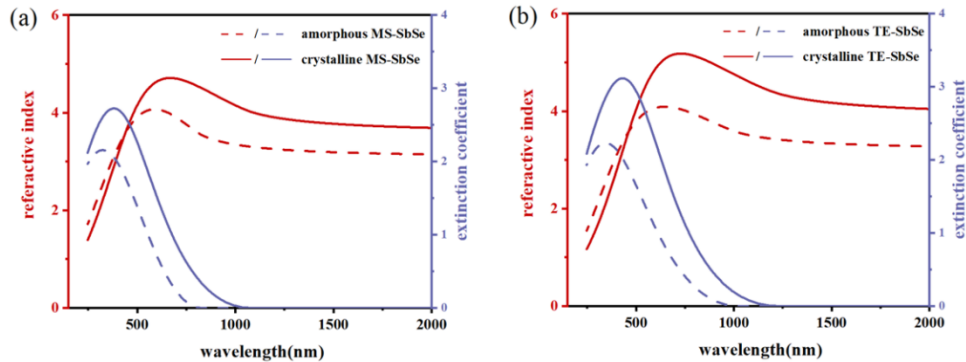


Fig. 4. Fitted ellipsometry results for (a) Sb-Se deposited by magnetron sputtering and (b) Sb-Se deposited by thermal evaporation in both amorphous (dashed lines) and crystalline (solid lines) phases.

Sb element is preferred to form resonant bonds in Sb-Se films than Se [39]. The formation of resonant bonds could increase the degree of electronic polarization, resulting in a large difference in the dielectric function of PCMs before and after phase switching [39]. This may be the main reason why Sb-rich Sb-Se films exhibit a larger optical contrast.

In order to verify the modulation effects of the Sb-Se phase-change films on photonic devices, we measured the transmission spectra of the Sb-Se-integrated microring resonators before and after annealing at 200 °C. We used a pair of grating couplers with -5 dB insertion loss at C-band for transmission spectrum collection. Figures 5(a) and (d) show the microring resonators' peak shifts induced by changes in extinction coefficients of Sb-Se patches with different lengths. As the length of the 30 nm-thick Sb-Se patch increases from 0 to 30 μm , resonant peaks of the micro-ring resonator gradually redshift. The Sb-Se-covered microring resonator could achieve a π -phase shift with an MS-SbSe patch length of 14.6- μm ($L_{\pi} = \lambda/2 \times (\Delta n_{eff})$) [40] and a TE-SbSe patch length of 9.3 μm , respectively, suggesting a more efficient phase-shifting capability of thermal-evaporated Sb-Se due to its larger optical contrast.

In order to quantitatively analyze the phase modulation effect and propagation loss of the Sb-Se-covered silicon waveguide, we extracted the peak shift ($\Delta\lambda$) and the quality factor Q value of the Sb-Se-covered microring resonator and further calculated the waveguide loss and total contrast of Sb-Se thin film [40]. It could be seen from Figs. 5(b) and (e) that an amorphous-Sb-Se-patch-covered waveguide introduces negligible loss compared to a bare silicon waveguide. After the crystallization of Sb-Se patch, the calculated propagation loss is as low as 0.019 dB/ μm for the MS-SbSe-covered waveguide and 0.036 dB/ μm for the TE-SbSe-covered waveguide at 1550 nm wavelength, which is two orders of magnitude lower than the loss of crystalline $\text{Ge}_2\text{Sb}_2\text{Te}_5$ -covered waveguides (7.6 dB/ μm) reported previously [22]. The propagation loss of a waveguide originates from absorption loss and scattering loss. The Sb-Se intrinsic material absorption loss could be very low according to ellipsometry. However, rod-like crystalline grains of TE-SbSe thin films present longer grain boundaries (see AFM images in Fig. 1), which could be the main reason for the higher propagation loss of TE-SbSe-integrated silicon waveguide than its magnetron-sputtered counterpart.

Figures 5(c) and (f) show the contrast in optical properties of sputtered and evaporated Sb-Se films at ~ 1550 nm wavelength, extracted and calculated from the transmittance spectra of the different lengths of Sb-Se-patch-covered ring resonators. The microring resonators with different lengths of Sb-Se correspond to nine devices with different numbers. By extracting the change

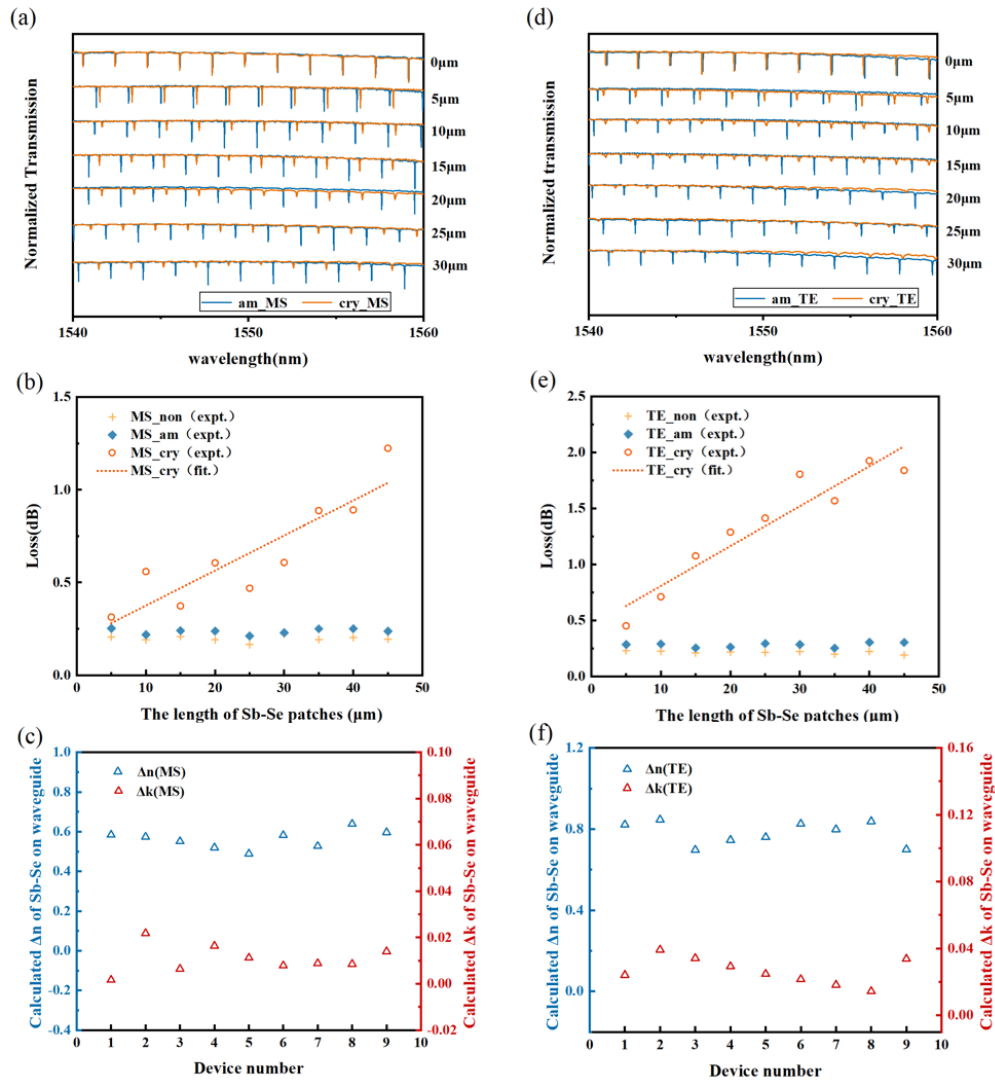


Fig. 5. (a), (d) Transmission spectra of microring response with different Sb-Se patch lengths deposited by magnetron sputtering and thermal evaporation, respectively. (b), (e) Measured losses of microring resonators with different Sb-Se patch lengths deposited by magnetron sputtering and thermal evaporation, respectively. “non” indicates the absence of Sb-Se. (c), (f) Calculated refractive index and extinction coefficient contrast for both amorphous and crystalline states of Sb-Se on waveguide at C-band.

of resonant-peak shift varying with the length of Sb-Se patches covered on ring resonators, we calculated the change of effective index (Δn_{eff}) of phase-change-integrated silicon waveguides. The refractive index change of Sb-Se films on waveguides could be then deduced by $\Delta n_{\text{eff}}/\Gamma$, where Γ is the mode confinement factor of the 1550-nm-wavelength fundamental transverse electric mode distributed in phase-change films. To make Γ as accurate as possible, the thickness of an Sb-Se patch was measured by AFM after the crystallization.

It could be seen from Figs. 5(c) and (f) that the calculated refractive index contrast between the amorphous and crystalline phase of TE-SbSe films fluctuates around 0.8, while which of MS-SbSe films fluctuates around 0.6 (with a fluctuation range ≤ 0.1). The result is consistent with the ellipsometry fitting, and the calculating error mainly derives from the fabrication error of devices and the slightly different thickness of phase-change films on different devices.

On the other hand, the calculated extinction coefficient contrast of Sb-Se films deposited by two approaches was also shown in Figs. 5(c) and (f), respectively. This extinction coefficient contrast, larger than the ellipsometry fitting result, is an “effective” one, since it is calculated from the propagating loss of phase-change-integrated waveguides and contains the scattering loss caused by grain boundaries and surface/sidewall roughness.

4. Conclusion

In this article, Sb-Se phase-change thin films were deposited via both thermal evaporation and magnetron sputtering. The crystal morphology, chemical composition and optical properties of Sb-Se films were characterized and studied, and the optical performance of Sb-Se patches on integrated silicon photonic waveguides was also verified. Thermal evaporated Sb-rich Sb-Se films present a large optical constant contrast ($\Delta n > 0.8$), achieving a π -phase shift with a length of 9.3 μm and thickness of 30 nm on silicon waveguide (i.e. $L_{\pi} < 10 \mu\text{m}$) without introducing noticeable optical loss ($< 0.04 \text{ dB}/\mu\text{m}$). The propagation loss of an Sb-Se-integrated silicon waveguide, although relatively low, mainly occurs at the crystalline state of PCM, originating from the scattering loss of grain boundaries. Hence, sputtered Se-rich Sb-Se thin can achieve even lower propagation loss ($< 0.02 \text{ dB}/\mu\text{m}$) in waveguides, likely due to smaller and more uniform grain boundaries in crystalline MS-SbSe films. It could be proved that the Sb-Se family is indeed a promising candidate for non-volatile photonic devices. Meanwhile, the influence of the properties of thin films on fast phase switching realized by laser and electrical pulses in photonic devices still needs to be further studied.

Funding. National Key Research and Development Program of China (2019YFB2203003, 2021YFB2801300); National Natural Science Foundation of China (91950204); Natural Science Foundation of Zhejiang Province (LD22F040002); State Key Laboratory on Integrated Optoelectronics (IOSKL2020KF05); Fundamental Research Funds for the Central Universities (2021QNA5007); Fundamental Research Funds for the Central Universities (2020XZZX005-07); Shanghai Sailing Program (19YF1435400).

Acknowledgements. The authors would like to acknowledge the fabrication support from ZJU Nano-Fabrication Center at Zhejiang University, Institute of Microelectronics of the Chinese Academy of Sciences and Westlake Center for Micro/Nano Fabrication and Instrumentation. The authors thanks State Key Laboratory of Chemical Engineering at Zhejiang University and Instrumentation and Service Center for Physical Sciences at Westlake University for supporting the film characterization and data interpretation. The authors would also like to thank Zihao Wang, Qing Zhao, Liming Shan and Jing He for their help in thin film preparation and characterization.

Disclosures. The authors declare no conflicts of interest.

Data availability. Data underlying the results presented in this paper are not publicly available at this time but may be obtained from the authors upon reasonable request.

Supplemental document. See [Supplement 1](#) for supporting content.

References

1. T. Siegrist, P. Merkelbach, and M. Wuttig, “Phase change materials: challenges on the path to a universal storage device,” *Annu. Rev. Condens. Matter Phys.* **3**(1), 215–237 (2012).

2. K. J. Miller, R. F. Haglund, and S. M. Weiss, "Optical phase change materials in integrated silicon photonic devices: review," *Opt. Mater. Express* **8**(8), 2415–2429 (2018).
3. Z. Yang and S. Ramanathan, "Breakthroughs in photonics 2014: phase change materials for photonics," *IEEE Photonics J.* **7**(3), 1–5 (2015).
4. C. Rios, M. Stegmaier, Z. Cheng, N. Youngblood, C. D. Wright, W. H. P. Pernice, and H. Bhaskaran, "Controlled switching of phase-change materials by evanescent-field coupling in integrated photonics [Invited]," *Opt. Mater. Express* **8**(9), 2455–2470 (2018).
5. Z. Fang, R. Chen, J. Zheng, and A. Majumdar, "Non-volatile reconfigurable silicon photonics based on phase-change materials," *IEEE J. Sel. Top. Quantum Electron.* **28**(3), 1–17 (2022).
6. C. Wu, H. Yu, H. Li, X. Zhang, I. Takeuchi, and M. Li, "Low-loss integrated photonic switch using subwavelength patterned phase change material," *ACS Photonics* **6**(1), 87–92 (2019).
7. P. Xu, J. Zheng, J. K. Doylend, and A. Majumdar, "Low-loss and broadband nonvolatile phase-change directional coupler switches," *ACS Photonics* **6**(2), 553–557 (2019).
8. D. Tanaka, Y. Shoji, M. Kuwahara, X. M. Wang, K. Kintaka, H. Kawashima, T. Toyosaki, Y. Ikuma, and H. Tsuda, "Ultra-small, self-holding, optical gate switch using $\text{Ge}_2\text{Sb}_2\text{Te}_5$ with a multi-mode Si waveguide," *Opt. Express* **20**(9), 10283–10294 (2012).
9. J. Zheng, Z. Fang, C. Wu, S. Zhu, P. Xu, J. K. Doylend, S. Deshmukh, E. Pop, S. Dunham, M. Li, and A. Majumdar, "Nonvolatile electrically reconfigurable integrated photonic switch enabled by a silicon PIN diode heater," *Adv. Mater.* **32**(31), 2001218 (2020).
10. N. Youngblood, C. Ríos, E. Gemo, J. Feldmann, Z. Cheng, A. Baldycheva, W. H. P. Pernice, C. D. Wright, and H. Bhaskaran, "Tunable volatility of $\text{Ge}_2\text{Sb}_2\text{Te}_5$ in integrated photonics," *Adv. Funct. Mater.* **29**(11), 1807571 (2019).
11. Z. Cheng, C. Rios, N. Youngblood, C. D. Wright, W. H. P. Pernice, and H. Bhaskaran, "Device-level photonic memories and logic applications using phase-change materials," *Adv. Mater.* **30**(32), 1802435 (2018).
12. X. Li, N. Youngblood, C. Ríos, Z. Cheng, C. D. Wright, W. H. P. Pernice, and H. Bhaskaran, "Fast and reliable storage using a 5 bit, nonvolatile photonic memory patch," *Optica* **6**(1), 1–6 (2019).
13. E. Gemo, J. Faneca, S. G.-C. Carrillo, A. Baldycheva, W. H. P. Pernice, H. Bhaskaran, and C. D. Wright, "A plasmonically enhanced route to faster and more energy-efficient phase-change integrated photonic memory and computing devices," *J. Appl. Phys.* **129**(11), 110902 (2021).
14. D. Kuzum, R. G. Jeyasingh, B. Lee, and H. S. Wong, "Nanoelectronic programmable synapses based on phase change materials for brain-inspired computing," *Nano Lett.* **12**(5), 2179–2186 (2012).
15. Z. Cheng, C. Rios, W. H. P. Pernice, C. D. Wright, and H. Bhaskaran, "On-chip photonic synapse," *Sci. Adv.* **3**(9), 1700160 (2017).
16. I. Chakraborty, G. Saha, and K. Roy, "Photonic in-memory computing primitive for spiking neural networks using phase-change materials," *Phys. Rev. Appl.* **11**(1), 014063 (2019).
17. X. Sui, Q. Wu, J. Liu, Q. Chen, and G. Gu, "A review of optical neural networks," *IEEE Access* **8**, 70773–70783 (2020).
18. M. Y. Shalaginov, S. An, Y. Zhang, F. Yang, P. Su, V. Liberman, J. B. Chou, C. M. Roberts, M. Kang, C. Rios, Q. Du, C. Fowler, A. Agarwal, K. A. Richardson, C. Rivero-Baleine, H. Zhang, J. Hu, and T. Gu, "Reconfigurable all-dielectric metalens with diffraction-limited performance," *Nat Commun* **12**(1), 1225 (2021).
19. Q. Wang, E. T. F. Rogers, B. Gholipour, C.-M. Wang, G. Yuan, J. Teng, and N. I. Zheludev, "Optically reconfigurable metasurfaces and photonic devices based on phase change materials," *Nat. Photonics* **10**(1), 60–65 (2016).
20. F. Ding, Y. Yang, and S. I. Bozhevolnyi, "Dynamic metasurfaces using phase-change chalcogenides," *Adv. Opt. Mater.* **7**(14), 1801709 (2019).
21. M. N. Julian, C. Williams, S. Borg, S. Bartram, and H. J. Kim, "Reversible optical tuning of GeSbTe phase-change metasurface spectral filters for mid-wave infrared imaging," *Optica* **7**(7), 746–754 (2020).
22. J. Zheng, A. Khanolkar, P. Xu, S. Colburn, S. Deshmukh, J. Myers, J. Frantz, E. Pop, J. Hendrickson, J. Doylend, N. Boechler, and A. Majumdar, "GST-on-silicon hybrid nanophotonic integrated circuits: a non-volatile quasi-continuously reprogrammable platform," *Opt. Mater. Express* **8**(6), 1551–1561 (2018).
23. Y. Zhang, J. B. Chou, J. Li, H. Li, Q. Du, A. Yadav, S. Zhou, M. Y. Shalaginov, Z. Fang, H. Zhong, C. Roberts, P. Robinson, B. Bohlin, C. Rios, H. Lin, M. Kang, T. Gu, J. Warner, V. Liberman, K. Richardson, and J. Hu, "Broadband transparent optical phase change materials for high-performance nonvolatile photonics," *Nat. Commun.* **10**(1), 4279 (2019).
24. J. Faneca, I. Zeimpekis, S. T. Ilie, T. D. Bucio, K. Grabska, D. W. Hewak, and F. Y. Gardes, "Towards low loss non-volatile phase change materials in mid index waveguides," *Neuromorph. Comput. Eng.* **1**(1), 014004 (2021).
25. J. Wu, M. Wei, J. Mu, H. Ma, C. Zhong, Y. Ye, C. Sun, B. Tang, L. Wang, J. Li, X. Xu, B. Liu, L. Li, and H. Lin, "High-performance waveguide-integrated $\text{Bi}_2\text{O}_2\text{Se}$ photodetector for Si photonic integrated circuits," *ACS Nano* **15**(10), 15982–15991 (2021).
26. C. Zhong, Z. Zhang, H. Ma, M. Wei, Y. Ye, J. Wu, B. Tang, P. Zhang, R. Liu, J. Li, L. Li, X. Hu, K. Liu, and H. Lin, "Silicon thermo-optic switches with graphene heaters operating at mid-infrared waveband," *Nanomaterials* **12**(7), 1083 (2022).
27. C. Chen, W. Li, Y. Zhou, C. Chen, M. Luo, X. Liu, K. Zeng, B. Yang, C. Zhang, J. Han, and J. Tang, "Optical properties of amorphous and polycrystalline Sb_2Se_3 thin films prepared by thermal evaporation," *Appl. Phys. Lett.* **107**(4), 043905 (2015).

28. S. Chen, X. Hu, J. Tao, J. Xue, G. Weng, J. Jiang, X. Shen, and S. Chen, "Effects of substrate temperature on material and photovoltaic properties of magnetron-sputtered Sb_2Se_3 thin films," *Appl. Opt.* **58**(11), 2823–2827 (2019).
29. M. Delaney, I. Zeimpekis, D. Lawson, D. W. Hewak, and O. L. Muskens, "A new family of ultralow loss reversible phase-change materials for photonic integrated circuits: Sb_2S_3 and Sb_2Se_3 ," *Adv. Funct. Mater.* **30**(36), 2002447 (2020).
30. A. Shongalova, M. R. Correia, J. P. Teixeira, J. P. Leitão, J. C. González, S. Ranjbar, S. Garud, B. Vermang, J. M. V. Cunha, P. M. P. Salomé, and P. A. Fernandes, "Growth of Sb_2Se_3 thin films by selenization of RF sputtered binary precursors," *Sol. Energy Mater. Sol. Cells* **187**, 219–226 (2018).
31. S. Polivtseva, J. O. Adegite, J. Kois, D. Mamedov, S. Z. Karazhanov, J. Maricheva, and O. Volobujeva, "A novel thermochemical metal halide treatment for high-performance Sb_2Se_3 photocathodes," *Nanomaterials* **11**(1), 52 (2020).
32. Y. Zhou, M. Leng, Z. Xia, J. Zhong, H. Song, X. Liu, B. Yang, J. Zhang, J. Chen, K. Zhou, J. Han, Y. Cheng, and J. Tang, "Solution-processed antimony selenide heterojunction solar cells," *Adv. Energy Mater.* **4**(8), 1301846 (2014).
33. K. Nagata, K. Ishibashi, and Y. Miyamoto, "Raman and infrared-spectra of rhombohedral selenium," *Jpn. J. Appl. Phys.* **20**(3), 463–469 (1981).
34. C. Chen, Y. Zhao, S. C. Lu, K. H. Li, Y. Li, B. Yang, W. H. Chen, L. Wang, D. B. Li, H. Deng, F. Yi, and J. Tang, "Accelerated optimization of $\text{TiO}_2/\text{Sb}_2\text{Se}_3$ thin film solar cells by high-throughput combinatorial approach," *Adv. Energy Mater.* **7**(20), 1700866 (2017).
35. Y. Li, Y. Zhou, J. Luo, W. Chen, B. Yang, X. Wen, S. Lu, C. Chen, K. Zeng, H. Song, and J. Tang, "The effect of sodium on antimony selenide thin film solar cells," *RSC Adv.* **6**(90), 87288–87293 (2016).
36. R. Browning, N. Kuperman, B. Moon, and R. Solanki, "Atomic layer growth of InSe and Sb_2Se_3 layered semiconductors and their heterostructure," *Electronics* **6**(2), 27 (2017).
37. X. Liu, J. Chen, M. Luo, M. Leng, Z. Xia, Y. Zhou, S. Qin, D. J. Xue, L. Lv, H. Huang, D. Niu, and J. Tang, "Thermal evaporation and characterization of Sb_2Se_3 thin film for substrate $\text{Sb}_2\text{Se}_3/\text{CdS}$ solar cells," *ACS Appl. Mater. Interfaces* **6**(13), 10687–10695 (2014).
38. V. Piacente, P. Scardala, and D. Ferro, "Total Vapor-Pressure of Solid Sb_2Se_3 ," *J. Mater. Sci. Lett.* **11**(12), 855–857 (1992).
39. K. Shportko, S. Kremers, M. Woda, D. Lencer, J. Robertson, and M. Wuttig, "Resonant bonding in crystalline phase-change materials," *Nat. Mater.* **7**(8), 653–658 (2008).
40. H. Lin, Y. Song, Y. Huang, D. Kita, S. Deckoff-Jones, K. Wang, L. Li, J. Li, H. Zheng, Z. Luo, H. Wang, S. Novak, A. Yadav, C.-C. Huang, R.-J. Shiue, D. Englund, T. Gu, D. Hewak, K. Richardson, J. Kong, and J. Hu, "Chalcogenide glass-on-graphene photonics," *Nat. Photonics* **11**(12), 798–805 (2017).